Mon. Not. R. Astron. Soc. **000**, 000–000 (0000) Printed August 9, 2016 (MN LATEX style file v2.2)

The Outburst Decay of the Low Magnetic Field Magnetar SWIFT J1822.3-1606: Phase-resolved Analysis and Evidence for a Variable Cyclotron Feature

Guillermo A. Rodríguez Castillo,[1,2] Gian Luca Israel,[1] Andrea Tiengo,[3,4,5] David Salvetti,[3] Roberto Turolla,[6,7] Silvia Zane,[7] Nanda Rea,[8,9] Paolo Esposito,[3,10] Sandro Mereghetti,[3] Rosalba Perna,[11] Luigi Stella,[1] José A. Pons,[12] Sergio Campana,[13] Diego Götz,[14] and Sara Motta[15]

[1] *INAF – Osservatorio Astronomico di Roma, Via Frascati 33, I-00040, Monte Porzio Catone, Italy*
[2] *Dipartimento di Fisica, Sapienza Università di Roma, Piazzale Aldo Moro 5, I-00185, Rome, Italy*
[3] *INAF – IASF Milano, Via E. Bassini 15, I-20133 Milano, Italy*
[4] *Istituto Universitario di Studi Superiori, Piazza della Vittoria 15, I-27100 Pavia, Italy*
[5] *Istituto Nazionale di Fisica Nucleare, Sezione di Pavia, Via A. Bassi 6, I-27100 Pavia, Italy*
[6] *Dipartimento di Fisica e Astronomia, Università di Padova, Via Marzolo 8, I-35131, Padova, Italy*
[7] *Mullard Space Science Laboratory, University College London, Holmbury St. Mary, Dorking, Surrey, RH5 6NT, UK*
[8] *Astronomical Institute "Anton Pannekoek", University of Amsterdam, Postbus 94249, 1090 GE Amsterdam, The Netherlands*
[9] *Institute of Space Sciences (CSIC-IEEC), Campus UAB, Carrer de Can Magrans, s/n, 08193 Barcelona, Spain*
[10] *Harvard–Smithsonian Center for Astrophysics, 60 Garden Street, Cambridge, MA 02138, USA*
[11] *Department of Physics and Astronomy, Stony Brook University, Stony Brook, NY, 11794, USA*
[12] *Departament de Física Aplicada, Universitat d'Alacant, Ap. Correus 99, 03080, Alacant, Spain*
[13] *INAF – Osservatorio Astronomico di Brera, Via E. Bianchi 46, I-23807, Merate, Italy*
[14] *AIM (CEA/DSM-CNRS-Université Paris Diderot), Irfu/Service d'Astrophysique, Saclay, F-91191 Gif-sur-Yvette, France*
[15] *ESAC, European Space Astronomy Centre, Villanueva de la Cañada, E-28692 Madrid, Spain*

arXiv:1510.09157v1 [astro-ph.HE] 30 Oct 2015

MNRAS, accepted October 2015

ABSTRACT

We study the timing and spectral properties of the low-magnetic field, transient magnetar SWIFT J1822.3-1606 as it approached quiescence. We coherently phase-connect the observations over a time-span of ∼500 days since the discovery of SWIFT J1822.3-1606 following the *Swift*-BAT trigger on 2011 July 14, and carried out a detailed pulse phase spectroscopy along the outburst decay. We follow the spectral evolution of different pulse phase intervals and find a phase and energy-variable spectral feature, which we interpret as proton cyclotron resonant scattering of soft photon from currents circulating in a strong ($\gtrsim 10^{14}$ G) small-scale component of the magnetic field near the neutron star surface, superimposed to the much weaker ($\sim 3 \times 10^{13}$ G) magnetic field. We discuss also the implications of the pulse-resolved spectral analysis for the emission regions on the surface of the cooling magnetar.

Key words: stars: neutron – stars: magnetar – star: individual (SWIFT J1822.3-16066) – X-rays: bursts

1 INTRODUCTION

Magnetars are isolated neutron stars believed to possess very strong magnetic fields ($\sim 10^{14}$ – 10^{15} G; Duncan & Thompson 1992; Thompson & Duncan 1995) which power their bright X-ray emission, as well as their occasional outbursts and flares. The magnetar class is historically composed of two classes of sources, the Anomalous X-ray Pulsars (AXPs) and Soft γ-ray Repeaters (SGRs), which share a wide range of characteristics, mainly (see Mereghetti 2008 for a review):

- spin periods in the 2 – 12 s range;
- large positive period derivatives (10^{-13} – 10^{-10} ß);
- X-ray luminosities in the range 10^{33} – 10^{35} erg s^{-1};
- sporadic bursting activity on timescales from ms to minutes.

While a decade ago their persistent X-ray emission (outside their bursting periods) was believed to be steady. In 2004

Ibrahim et al. (2004) discovered the first transient magnetar, XTE J1810-197. The source was observed at a peak persistent luminosity $\sim$ 100 higher that the quiescent value ($\sim 10^{33}$ erg s^{-1}; Gotthelf et al. 2004). Other magnetars have since been discovered which undergo transient outbursts lasting months to years until the quiescence is recovered. Therefore many unidentified faint X-ray sources might host quiescent magnetars that can be identified as they become active. Thanks to the observing capabilities of present space missions such as *Swift*, *INTEGRAL* and *Fermi*, several new magnetars have been discovered through the detection of short bursts events (10-100 ms duration) and/or long-term (months–years) outbursts (see Rea & Esposito 2011 for a review).

The magnetic field strength of magnetars is usually estimated by assuming that, like ordinary pulsars, they spin down mainly through magnetic dipole losses. The intensity of the dipole magnetic field at the star equator is estimated as: $B_{dip} \sim 3.2 \times 10^{19}(P\dot{P})^{1/2}$ G, where P is the spin period in seconds, $\dot{P}$ its first time derivative and a neutron star with radius $R \sim 10^6$cm and moment of inertia 10^{45} g cm^2 is assumed.

Until some years ago all such measurements led to dipolar field strengths of $\sim 10^{14}$–10^{15} G. However, the monitoring of the outburst of SGR 0418+5729 demonstrated the existence of sources showing typical magnetar-like outbursts and short bursts, but with dipole fields in line with ordinary pulsars (i.e. $\sim 6 \times 10^{12}$ G; Rea et al. 2013). Simulations of magnetic field evolution in neutron stars with different initial field strength and configuration have shown that, a relatively old magnetar such as SGR 0418+5729 despite its low surface dipolar field, might still harbor a sufficiently intense internal/crustal toroidal field to give rise to outbursts and short X-ray bursts (Turolla et al. 2011).

Two more low-field magnetars were recently discovered thanks to their outburst activity, 3XMM J185246.6+003317 (Zhou et al. 2014, Rea et al. 2014) and SWIFT J1822.3-1606 (Rea et al. 2012; Scholtz et al. 2012). The latter source was studied through the long-term monitoring that we present in this work.

1.1 SWIFT J1822.3-1606

The magnetar SWIFT J1822.3-1606 (Swift J1822, hereafter) was discovered through the detection of a series of bursts by the *Swift* Burst Alert Telescope (BAT) and *Fermi* Gamma-ray Burst Monitor (GBM) (Cummings et al. 2011) in July 2011. Soon afterwards Pagani et al. (2011) found the position of the new source at RA (J2000): 18h 22m 18.00s Dec (J2000): -16d 04′ 26.8″, with 1.8 arcsec radius of uncertainty (90% confidence). Subsequently, the source was followed by virtually all the current generation of X-ray satellites. The results of the first 9 months of X-ray monitoring of this new magnetar were presented and discussed by Rea et al. (2012; hereafter R12), Scholz et al. (2012) and Scholz et al. (2014). In this work we perform an unprecedent coherent, pulse phase resolved spectroscopy (PPS) analysis spanning more than 400 days of outburst decay (see Fig. 2).

2 OBSERVATIONS AND DATA PROCESSING

For the study of the outburst decay we used data from one *XMM-Newton*, four *Chandra* and ten *Swift* observations in addition to the data used in R12. We also used the *Chandra* ACIS-S pointings carried out at the beginning of the outburst in order to perform a detailed time-resolved PPS study. A log of the data collected during 2012 is given in Table 1.

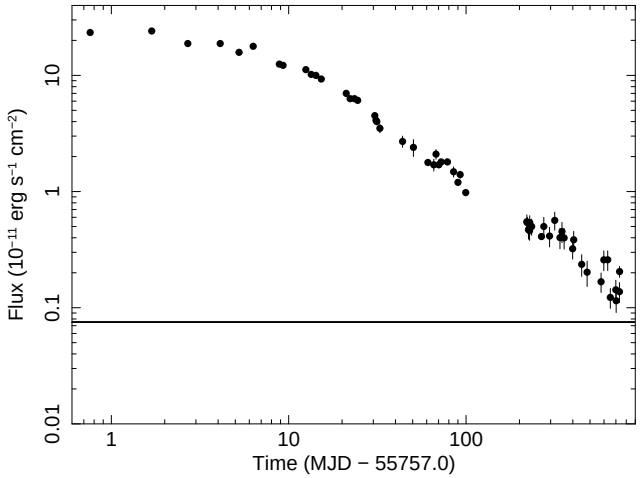

Figure 1. Swift-RXT flux decay of Swift J1822.3–1606 in the 1–10 keV energy range. The solid line represents the quiescence flux level.

The data reduction was performed by means of the standard procedures outlined in R12: it consists of initial raw data calibration, filtering from soft-proton flares, correcting the arrival times to the barycenter of the solar system, source and background extraction, pileup checks, spectral data rebinning and grouping (see Sec. 2.2.2 for datails). These steps were performed by using the official Science Analysis System (SAS) package (version 11) for the *XMM-Newton* data, and the Chandra Interactive Analysis of Observations (CIAO) system (version 4.4) for the *Chandra* data. The *Swift* data were processed and filtered with standard procedures and quality cuts[1] using FTOOLS tasks in the HEASOFT software package (v. 6.12) and the calibration files from the latest CALDB release.

For the spectral analysis we used XSPEC (version 12.7.1), for the timing analysis, XRONOS (version 5.22) and pipelines developed in-house for the phase fitting procedures.

2.1 Timing

We begun by extending the validity of the phase-coherent timing solution reported by R12 by adding the new datasets listed in Table 1. In fact, the accuracy and time span between the latest R12 observation and the first of the additional ones listed in Table 1 ($\sim$ 21 days) is such that we do not miss any cycle in the phase-fitting procedure.

In order to fit the additional data, we added a second period derivative to the timing solution (see Fig. 2, lower panel). The introduction of the higher order period derivative results in a significant improvement of the fit; an F-test gave a probability of $> 10\sigma$ that the inclusion of a cubic component is required for our data set (see Fig. 2).

The best timing solution for our data set is: $P = 8.437720019(7)$ s, $\dot{P} = 1.34(1) \times 10^{-13}$ s s^{-1} and $\ddot{P} = -5.1(2) \times 10^{-21}$ s s^{-2} (1σ c.l., 3 parameters of interest for epoch 55757.0 MJD; see also Table 2). Based on the best fitting P and $\dot{P}$, the inferred surface dipolar magnetic field is $B \sim 3.4(1) \times 10^{13}$ G at the equator. This value lies in between previous results of Scholz et al. (2012): $B \sim 5 \times 10^{13}$ G, and R12: $B \sim 2.7 \times 10^{13}$ G, and is

[1] See http://swift.gsfc.nasa.gov/docs/swift/analysis/ for more details.

Table 1. Observations used in the timing analysis. In bold are denoted the observations added to those used in R12.

Instrument	Obs.ID	Date[a] (MJD TBD)	Exposure (ks)
Swift	00032033001 (PC)	55757.75058	1.6
RXTE	96048-02-01-00	55758.48165	6.5
Swift	00032033002 (WT)	55758.68430	2.0
Swift	00032033003 (WT)	55759.69082	2.0
RXTE	96048-02-01-05	55760.80853	1.7
Swift	00032033005 (WT)	55761.54065	0.5
RXTE	96048-02-01-01	55761.55969	5.0
Swift	00032033006 (WT)	55762.24089	1.8
RXTE	96048-02-01-02	55762.47384	4.9
Swift	00032033007 (WT)	55763.30400	1.6
RXTE	96048-02-02-00	55764.61846	6.1
RXTE	96048-02-02-01	55765.46687	6.8
Swift	00032033008 (WT)	55765.85252	2.2
Swift	00032033009 (WT)	55766.28340	1.7
RXTE	96048-02-02-02	55767.59064	3.0
RXTE	96048-02-02-03	55769.35052	3.4
Swift	00032033010 (WT)	55769.49531	2.1
Swift	00032033011 (WT)	55770.39936	2.1
Chandra	13511	55770.83049	11.7
Swift	00032033012 (WT)	55771.23302	2.1
RXTE	96048-02-03-00	55771.34185	6.8
Swift	00032033013 (WT)	55772.40044	2.1
RXTE	96048-02-03-01	55774.34999	6.9
Chandra	12613	55777.22193	15.0
RXTE	96048-02-03-02	55777.85040	1.9
Swift	00032051001 (WT)	55778.10744	1.7
Swift	00032051002 (WT)	55779.18571	1.7
RXTE	96048-02-04-00	55780.85040	6.7
Swift	00032051003 (WT)	55780.49505	2.3
Swift	00032051004 (WT)	55781.49878	2.3
RXTE	96048-02-04-01	55782.57749	6.2
RXTE	96048-02-04-02	55784.97179	6.2
Swift	00032051005 (WT)	55786.42055	2.2
Swift	00032051006 (WT)	55787.58688	2.2
RXTE	96048-02-05-00	55788.05419	6.0
Swift	00032051007 (WT)	55788.25617	2.3
Swift	00032051008 (WT)	55789.66173	1.7
RXTE	96048-02-05-01	55789.95880	6.0
Swift	00032051009 (WT)	55790.36270	2.2
RXTE	96048-02-06-00	55794.45899	6.5
RXTE	96048-02-07-00	55799.61550	6.9
Swift	00032033015 (WT)	55800.86278	2.9
Swift	00032033016 (WT)	55807.48660	2.4
RXTE	96048-02-08-00	55810.37979	6.0
Suzaku/XIS	906002010	55817.92550	33.5
RXTE	96048-02-10-00	55820.23970	6.7
Chandra	12614	55822.79364	10.1
Swift	00032033017 (WT)	55822.82836	4.9
Swift	00032033018 (WT)	55824.71484	1.5
RXTE	96048-02-10-01	55826.18540	5.6
XMM-Newton	0672281801	55827.25350	10.6
Swift	00032033019 (WT)	55829.45421	2.3
Swift	00032033020 (WT)	55835.54036	2.6
RXTE	96048-02-11-00	55835.90370	7.0
Swift	00032033021 (WT)	55842.06040	4.2
RXTE	96048-02-12-00	55842.23269	5.8
XMM-Newton	0672282701	55847.06380	25.8
Swift	00032033022 (WT)	55849.61916	3.4
RXTE	96048-02-13-00	55849.6597976	5.6
Swift	00032033024 (WT)	55862.59155	10.2
RXTE	96048-02-14-00	55863.11100	5.6

Continues below.

Table 1. Continuation

Instrument	Obs.ID	Date[a] (MJD TBD)	Exposure (ks)
Chandra	12615	55867.17461	16.3
Swift	00032033025 (PC)	55977.16600	6.3
Swift	00032033026 (WT)	55978.53399	10.2
Swift	00032033027 (PC)	55981.99499	11.0
Swift	00032033028 (WT)	55982.96299	7.0
Swift	00032033029 (WT)	55985.17799	7.0
Swift	00032033030 (WT)	55985.55000	7.0
Swift	00032033031 (WT)	55991.09231	6.7
XMM-Newton	0672282901	56022.95692	26.9
Swift	00032033032 (WT)	56031.141159	4.3
Chandra	14330	56037.08846	20.1
Swift	00032033033	56052.66948	5.2
Swift	00032033034	56073.25354	4.9
Swift	00032033035	56095.56083	5.6
Swift	00032033036	56104.55201	6.2
Swift	00032033037	56114.31112	6.8
Swift	00032033038	56136.32359	9.0
Swift	00032033039	56156.20958	4.9
Swift	00032033040	56161.69589	5.0
XMM-Newton	0672283001	56178.85111	21.7
Swift	00032033042	56206.00752	5.0
Swift	00032033043	56238.70919	4.9

[a] Mid-point of the observations.

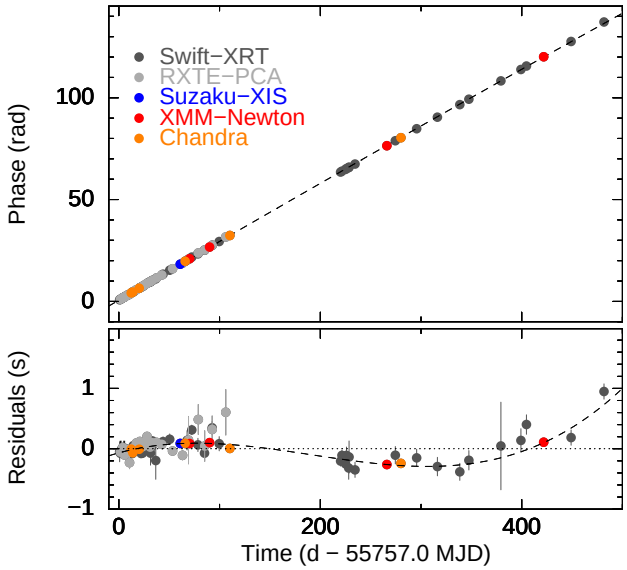

Figure 2. Pulse phase evolution over time. In the lower panel are shown the time residuals after correcting the linear and quadratic components (correction to the P and $\dot{P}$ values). The dashed line in the residual panel marks the detected $\ddot{P}$ component. The epoch of reference is 55757.0 Modified Julian Date (MJD). See the text for details on the ephemerides.

higher than the estimate of Scholz et al. (2014): $B \sim 1.4 \times 10^{13}$ G. Yet, it is lower then the B_{QED} critical value ($B \sim 4.4 \times 10^{13}$ G): SWIFT J1822.3-1606 is thus the magnetar with the second lowest magnetic field. This timing solution also implies a spin-down power $L_{rot} = 4\pi^2 I \dot{P}/P^3 \sim 9 \times 10^{30}$ erg s^{-1}, assuming uniform-density neutron star with moment of inertia $I = 10^{45}$ g cm^2. The inclusion of a third period derivative, or other components, such as a post glitch recovery, does not significantly improve the fit. How-

Table 2. Timing parameters for SWIFT J1822.3-1606.

Reference Epoch (MJD)	55757.0
Validity period (MJD)	55757– 56239
P (s)	$8.437720019(7)$
$\dot{P}$ ($\mathrm{s\,s^{-1}}$)	$1.34(1) \times 10^{-13}$
$\ddot{P}$ ($\mathrm{s\,s^{-2}}$)	$-5.1(2) \times 10^{-21}$
ν (Hz)	$0.1185154281(1)$
$\dot{\nu}$($\mathrm{s^{-2}}$)	$-1.88(2) \times 10^{-15}$
$\ddot{\nu}$($\mathrm{Hz\,s^{-2}}$)	$7.1(2) \times 10^{-23}$
χ^2/dof	168/81
RMS residuals (ms)	360
B (Gauss)	$\sim 3.4 \times 10^{13}$
$\mathrm{L_{rot}}$ ($\mathrm{erg\ s^{-1}}$)	$\sim 8.9 \times 10^{30}$
τ_c (Myr)	~ 1.0

ever, the timing solution by Scholz et al. (2014) over a longer – with respect to this work – time span of ~ 2.3 years did indeed improve with the inclusion of an exponential glitch recovery for the first ~ 60 days, and a separate P-$\dot{P}$ timing solution for the rest of the data set, see Scholz et al. (2014) for details on their solution. For the purpose of this work a single coherent timing solution for the entire data set is desirable and we use our timing solution to perform the pulse phase-resolved analysis. We note that the timing solutions with parameters closer to ours are those reported by R12 and the 2nd solution of Scholz et al. (2012), which were obtained over a time-span of ~ 1 year.

2.2 Spectral Analysis

2.2.1 Phase-average analysis

Phase-averaged spectral analysis were performed by R12, Scholz et al. (2012) and Scholz et al. (2014). In all cases a model composed by a photoelectrically absorbed blackbody (BB) plus a power-law (PL) was used to fit the spectra; in R12 a two-BB was used as well. In both Scholz et al. (2012) and Scholz et al. (2014), acceptable fits were obtained in the $1-10$ keV band. In R12 over the $0.6-10$ keV energy band (for both models). Restricting the *XMM-Newton* data to those energy intervals, we were able to reproduce their results for all the common *XMM-Newton* spectra. However, the situation changes when we considered a larger energy range, $0.3-10$ keV.

Indeed, the two-BB model failed to fit the high energy part ($>$ 6 keV) of the spectra (see e.g. Fig. 4, upper panel, where a $\chi^2_{red} = 2.31$ for 674 degrees of freedom, dof was obtained). Following the same rationale as in the case of CXOU J164710.2–455216 (Rodríguez Castillo et al. 2013), we added an additional ("cold") blackbody with fixed temperature to the two-BB model. Thus, adding one additional parameter to the fit, namely, the cold blackbody radius. This additional component is meant to account for a colder surface region, which might correspond to either the rest of the NS surface, or a portion of it. The $\mathrm{kT}_{BB} \sim 150$ eV value is based on spectral analysis of the quiescent emission of SWIFT J1822.3-1606, previously performed in R12 and Scholz et al. (2012). Note that estimates for other magnetars (i.e. XTE J1810–197 and CXOU J164710.2–455216, see Albano et al. 2010) yield similar values.

The addition of the colder BB yields an improved χ^2_{red} of 1.08 (670 dof) (see Fig. 4 and Table 3). We studied the significance of such component by calibrating the F-statistics using simulations

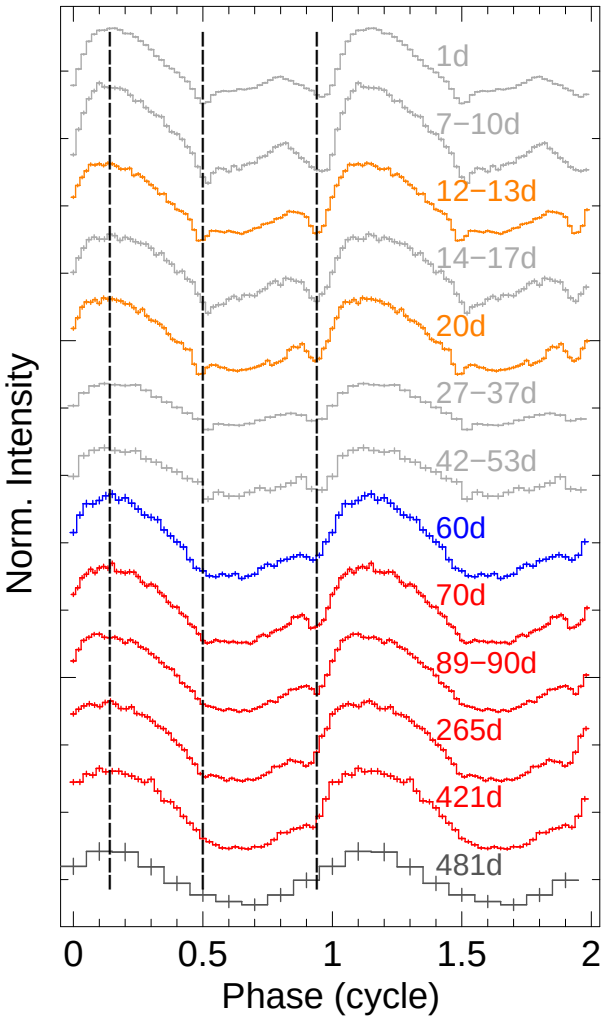

Figure 3. Selected pulse shapes plotted as a function of time for different epochs of the 2011-2012 outburst of SWIFT J1822.3-1606. The 1-10keV light curves (2-10keV for RXTE) have been folded to the $P-\dot{P}-\ddot{P}$ phase-coherent solution reported in Table 2. Different colors mark data from different missions similarly to the color code used in Figure 2.

of the null model (the double-blackbody model) as suggested by Protassov et al. (2002). In accordance with this approach, the distribution of the null F-statistic was produced by fitting each simulated spectrum with both the null and the triple-blackbody model and extracting the relative F-statistic. Running 5×10^5 Monte Carlo simulations, we obtained that the chance occurence probability of such an improvement is lower than 2×10^{-6}.

Beside significantly improving the fits, the 1(T-fixed)+2(free) BB (1+2BB, for short) model provides consistent results. First, the radius, which is the only free parameter of the additional, temperature-fixed BB, varies from $4.0\,d_{1.6}$ km to $7.3\,d_{1.6}$ km, where $d_{1.6}$ is the distance to the magnetar in units of 1.6 kpc, the value proposed by Scholz et al. (2012) (see below). Another hint at the validity of the model is the fact that the measured radius

SWIFT J1822.3-1606 1+2-blackbody phase-average spectral fit					
Obs. MJD	T_h (keV)	R^h_{BB} (Km)	T_w (keV)	R^w_{BB} (Km)	R^c_{BB} (Km)
15777	$1.07^{+0.04}_{-0.03}$	0.29 ± 0.02	0.52 ± 0.01	1.26 ± 0.04	11.6 ± 0.2
15827	$0.87^{+0.04}_{-0.03}$	0.23 ± 0.02	0.41 ± 0.02	$0.96^{+0.05}_{-0.04}$	7.0 ± 0.3
15846	0.83 ± 0.03	0.22 ± 0.01	0.41 ± 0.02	0.82 ± 0.04	6.3 ± 0.3
16023	0.87 ± 0.03	$0.10^{+0.02}_{-0.01}$	0.42 ± 0.02	$0.54^{+0.02}_{-0.03}$	4.52 ± 0.2
16178	$0.98^{+0.10}_{-0.08}$	$0.05^{+0.02}_{-0.01}$	0.48 ± 0.02	$0.36^{+0.02}_{-0.03}$	4.2 ± 0.2

Table 3. Parameters of 1+2BB fit of *Chandra* (MJD 15777) and *XMM-Newton* spectra (See text for details on the model). The distance used to calculate the R_{BB} was 1.6 kpc, as proposed by Scholz et al. (2012). Error are 1-σ.

of the cold component is consistent with the BB radius observed in quiescence, before the outburst, at the same temperature (R12, Scholz et al. 2012). Note as well that the measured radius, both in our analysis as well as in the cited papers, is significantly less then the expected ~ 10 km for a neutron star, suggesting that it may not correspond to the whole surface.

On the other hand, the PL+BB model, while fitting well the data in the 0.6–10 keV range (R12), shows significant residuals at lower energies < 0.6 keV (see Fig. 4, middle panel). In the 0.3–10 keV range the PL+BB model yields a poor χ^2_{red} /dof $= 1.44$ /674. In the case of the PL+BB model, adding the same temperature-fixed BB, as it was done for the 2BB model, only marginally improves the fit (χ^2_{red} /dof $= 1.22$ /670).

Using the best 1(T-fixed)+2(free) BB model and the whole set of phase-average spectra, we obtained a best-fit column density value of $N_{\rm H} = 4.7(1) \times 10^{21}$ cm^{-2}, which is very close to the values found in previous works, R12 $N_{\rm H} = 5.0(1) \times 10^{21}$ cm^{-2} ; and Scholz et al. (2012) $N_{\rm H} = 4.5(1) \times 10^{21}$ cm^{-2}. Moreover, this value is consistent with the $N_{\rm H} = 4(1) \times 10^{21}$ cm^{-2} of the Galactic HII region M17 (Townsley et al. 2003), located about 20′ from Swift J1822 and at 1.6 ± 0.3 kpc from us (Nielbock et al. 2001), as noted by Scholz et al. (2012). We kept $N_{\rm H}$ fixed at 4.7×10^{21} cm^{-2} for the rest of the analysis, and adopted a tentative distance of 1.6 kpc in BB radii calculations.

For this analysis the solar abundances by Anders & Grevesse (1989) were used to account for the photoelectric absorption, the same used in all previous analysis (R12, Scholz et al. 2012). In addition, we used the same photoelectric cross-sections by Balucinska-Church & McCammon (1992) used in the cited works. We also tried other solar abundances (Feldman (1992); Wilms et al. (2000); Lodders (2003) and Asplund et al. (2009)) and in all cases the 1+2BB model showed a similar statistical predominance in comparision to the PL+BB and the 2BB models as described above.

2.2.2 Coherent phase-resolved analysis

In this section we describe a pulse phase resolved analysis as a function of the decaying flux by using one *Chandra* plus the four *XMM-Newton* pointings covering the outburst decay from day 12 up to day 421. To do so, we use our updated phase-coherent timing solution to fold and extract the spectra.

In order to define the phase interval selection we inspected spectral changes across the pulse profile in single observations (see e.g. Fig. 5). A pulse profile comparison as a function of time is shoen in Fig. 6. In both figures similar features are seen in the same phase regions, near phase 0.5 and 0.93. Based on this and in order to make sure that each phase interval contains enough counts, we adopted the phase intervals marked as P1, P2, P3 and P4 in Fig. 6, which correspond to phases 0.05-0.4, 0.4-0.55, 0.55-0.9 and 0.9-1.05, respectively.

For the spectral fitting (with XSPEC version 12.7.1), the data were grouped so as to have at least 30 counts per energy bin, while the instrument energy resolution were oversampled by a factor of three. The standard routines of XMM-SAS and CIAO were used to produce the ancillary response files and redistribution matrix files.

For the phase-resolved spectroscopy, we used the 2(free)+1(T-fixed) BB model described above (Section 2.2.1). We also assume that the geometric configuration of the emission zones does not vary dramatically during the outburst decay, so we follow each evolving component during the outburst decay. The observed pulse profile relative stability over time (see e.g. Fig. 6) indicates that these assumptions are reasonable. In the context of our spectral analysis, we interpret the flux evolution (Fig. 1) as changes in the radii and temperature of the two free blackbodies. Since no geometric information about the specific configuration of the emission zones is available, the two blackbodies were left free to vary from phase to phase, in the case that more then one hot region is present. We favor a two-hotspot (emission zones) model (see Section 3), since a single hotspot configuration does not reproduce the observed pulse profiles. The results are presented in Table 4 and graphically in Figs. 7, 8 and 9, where phase intervals P1 and P3 are shown in the upper panels and P2 and P4 in the lower panels. The phase intervals have been divided in this way for visualization purposes and because of similarities found in some intervals, in particular, between P2 and P4, which show quite similar values and evolution throughout the outburst decay (see Section 3).

In order to maintain coherence with previous works and with our phase-averaged analysis, we used the Anders & Grevesse (1989) solar abundances and corrected the photoelectric absorption with Balucinska-Church & McCammon (1992) photoelectric cross-sections in the pulse-phase resolved spectroscopy as well. We note that since different solar abundances affect only the lower energies, only the radius of the fixed, cold BB, is affected (reduced it by a factor of $\lesssim 2$). The warm and hot BB, (see Table 4) remain unaffected within the 1-σ confidence interval, when the solar abundances are varied (see also Section 2.2.1).

SWIFT J1822.3-1606: 1+2-blackbody spectral fit						
Pulse phase interval[a]	Obs. MJD	T_h (keV)	R^h_{BB} (km)	T_w (keV)	R^w_{BB} (km)	R^c_{BB} (km)[b]
	15777	$1.24^{+0.08}_{-0.07}$	$0.26^{+0.04}_{-0.03}$	$0.56^{+0.01}_{-0.02}$	1.48 ± 0.04	14.5 ± 0.3
	15827	$0.95^{+0.04}_{-0.03}$	$0.23^{+0.03}_{-0.02}$	0.46 ± 0.02	1.01 ± 0.05	8.9 ± 0.2
P1	15846	0.89 ± 0.03	0.22 ± 0.02	0.43 ± 0.02	$0.94^{+0.06}_{-0.05}$	7.8 ± 0.2
$\chi^2_{red} = 1.1865$	16023	0.84 ± 0.03	0.14 ± 0.02	0.44 ± 0.02	$0.68^{+0.05}_{-0.04}$	5.1 ± 0.1
	16178	$0.94^{+0.10}_{-0.08}$	$0.07^{+0.03}_{-0.02}$	0.46 ± 0.02	0.44 ± 0.03	4.6 ± 0.1
	15777	$1.05^{+0.10}_{-0.08}$	$0.25^{+0.05}_{-0.07}$	0.48 ± 0.03	$1.19^{+0.12}_{-0.08}$	11.2 ± 0.4
	15827	$0.89^{+0.06}_{-0.05}$	0.19 ± 0.03	0.38 ± 0.04	$1.0^{+0.2}_{-0.1}$	6.9 ± 0.4
P2	15846	$0.82^{+0.05}_{-0.04}$	0.19 ± 0.03	0.39 ± 0.03	$0.79^{+0.14}_{-0.09}$	6.0 ± 0.3
$\chi^2_{red} = 1.0522$	16023	$1.0^{+0.2}_{-0.1}$	$0.06^{+0.04}_{-0.02}$	$0.47^{+0.03}_{-0.04}$	$0.38^{+0.05}_{-0.04}$	4.5 ± 0.2
	16178	$1.0^{+0.9}_{-0.2}$	$0.02^{+0.13}_{-0.01}$	$0.50^{+0.05}_{-0.07}$	$0.29^{+0.06}_{-0.03}$	4.1 ± 0.2
	15777	$0.89^{+0.04}_{-0.03}$	0.38 ± 0.04	0.43 ± 0.03	$1.27^{+0.12}_{-0.09}$	11.2 ± 0.3
	15827	0.75 ± 0.02	0.28 ± 0.02	0.33 ± 0.03	$1.1^{+0.2}_{-0.1}$	6.0 ± 0.3
P3	15846	$0.76^{+0.03}_{-0.02}$	0.22 ± 0.02	0.36 ± 0.03	$0.75^{+0.12}_{-0.08}$	5.6 ± 0.2
$\chi^2_{red} = 1.0516$	16023	$0.93^{+0.09}_{-0.07}$	$0.07^{+0.02}_{-0.01}$	0.43 ± 0.03	$0.41^{+0.04}_{-0.03}$	4.5 ± 0.1
	16178	> 0.67	$0.002^{+0.029}_{-0.002}$	$0.55^{+0.01}_{-0.03}$	$0.24^{+0.02}_{-0.01}$	4.4 ± 0.1
	15777	$1.00^{+0.09}_{-0.07}$	$0.30^{+0.08}_{-0.06}$	$0.51^{+0.02}_{-0.03}$	$1.38^{+0.08}_{-0.06}$	11.4 ± 0.5
	15827	0.78 ± 0.03	$0.32^{+0.04}_{-0.03}$	0.35 ± 0.03	$1.4^{+0.3}_{-0.2}$	7.0 ± 0.5
P4	15846	$0.80^{+0.09}_{-0.06}$	$0.23^{+0.07}_{-0.06}$	0.44 ± 0.05	$0.76^{+0.13}_{-0.07}$	7.6 ± 0.3
$\chi^2_{red} = 1.0516$	16023	$0.91^{+0.10}_{-0.07}$	$0.09^{+0.03}_{-0.02}$	0.42 ± 0.03	$0.57^{+0.07}_{-0.05}$	4.8 ± 0.2
	16178	$1.0^{+0.3}_{-0.2}$	$0.04^{+0.05}_{-0.02}$	$0.48^{+0.03}_{-0.04}$	$0.37^{+0.05}_{-0.03}$	4.5 ± 0.2

[a] See Fig. 6 for reference.

[b] Different solar abundances can reduce this value up to a factor of ~ 2. See alsoSection 2.2.1

Table 4. 1+2BB fit spectral parameters of the phase resolved spectroscopy. The distance used to calculate the R_{BB} was 1.6 kpc, as proposed by Scholz et al. (2012). Reported error are 1-σ.

2.2.3 Phase-variable spectral features

To better explore the complex variability with phase of the X-ray spectrum of SWIFT J1822.3-1606, we created phase-energy images from the X-ray observations with the best counting statistics and enough spectral/time resolution, by binning the source counts into small phase and energy intervals (see Figs. 10 and 11). This kind of analysis has proven useful to identify possible narrow spectral features that strongly vary with phase, like the absorption-like feature discovered in SGR 0418+5729 (Tiengo et al. 2013; hereafter T13).

A dark straight line, slightly inclined to the right, is visible at phase $\sim$0.5 in the *RXTE*, *Chandra* and *XMM-Newton* images (Figs. 10 and 11). In addition, the uppermost panel of Fig. 11 obtained with RXTE data of energies > 4 keV, displays a dark 'V'at phase $\sim 0.9 - 1.1$, similar to the one detected in the phase-energy images of SGR 0418+5729 (T13). The same feature cannot be clearly detected in the *Chandra* and *XMM-Newton* data likely due to poorer statistics at high energies.

These dark tracks are rather narrow and almost vertical, suggesting the presence of an absorption-like line in the spectrum, whose energy rapidly varies with phase. As in T13, 50 phase-resolved spectra for each of the three datasets were extracted and analyzed with simple spectral models. Due to the relatively small number of counts in each phase interval, all the *XMM-Newton* spectra were consistent with the model of the phase-averaged spectrum, simply rescaled by a flux normalization factor. On the other hand, the *RXTE* phase-resolved spectra displayed significant differences, which motivated a detailed analysis.

A template spectral model was derived by fitting the *RXTE*/PCA spectrum extracted from the 0.6–0.8 phase interval, where the phase-energy image shows no narrow-band spectral variability. For consistency with the previous analysis, we adopted a three blackbody model with photoelectric absorption fixed at $N_{\rm H} = 4.7 \times 10^{21}$ cm^{-2} and one of the three blackbody components with $kT = 150$ eV and $R_{\rm BB} = 10$ km (assuming a distance of 1.6 kpc).[2] A good fit is obtained only by adding a Gaussian emission line with $E = 6.47 \pm 0.06$ keV, $\sigma = 0.3 \pm 0.1$

[2] Since the PCA spectra are analyzed only for $E > 2.5$ keV, this soft blackbody component gives a negligible contribution to the spectral fit.

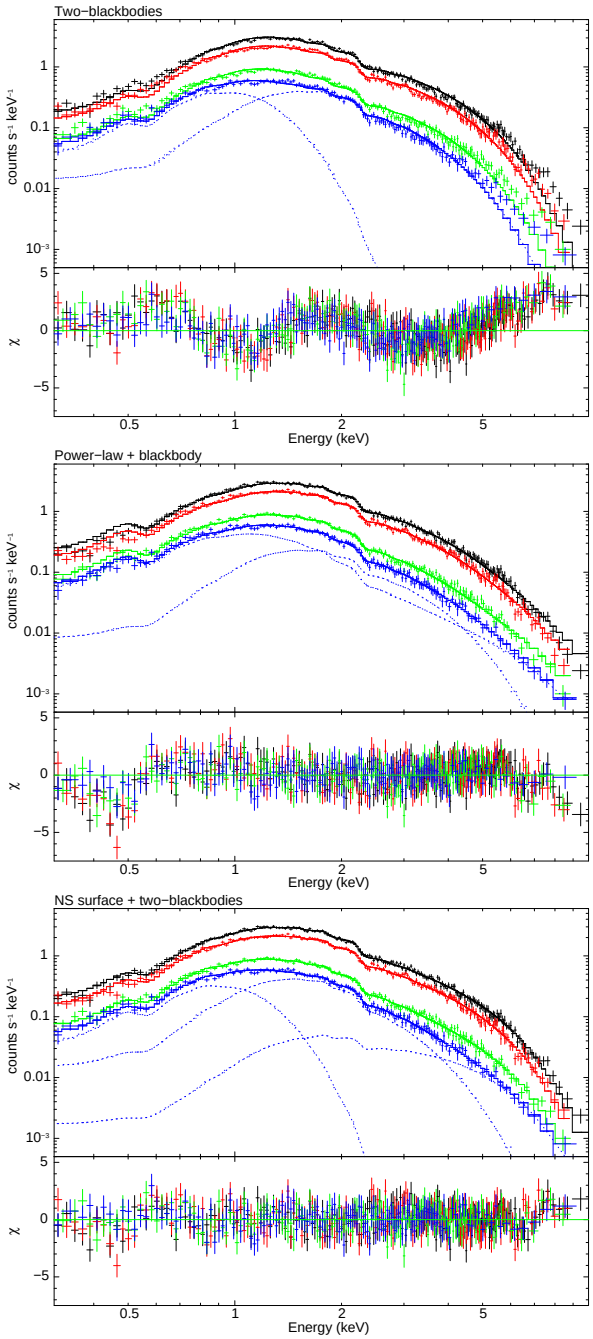

Figure 4. SWIFT J1822.3-1606 *XMM-Newton* spectra. Best fits using 2-blackbodies (upper panel), blackbody plus power-law (middle panel), and 2+1-blackbodies (lower panel). $\chi^2_{red} = 2.31, 1.44$ and 1.08, respectively. The fits components of the last observations (blue dotted lines) are shown for comparison. Note that by the last observation the source has significantly softened and the hot BB component is not dominant. See the text for details.

keV and flux of $(4 \pm 1) \times 10^{-4}$ photons cm^{-2} s^{-1}, possibly due to an incorrect reconstruction of the Galactic Ridge component in the PCA background model. In this case, the temperatures of the two variable blackbody components are: $kT_h = 1.7 \pm 0.1$ keV and $kT_w = 0.73 \pm 0.02$ keV. As can be seen in the lowermost panel of Fig. 12, this template model rescaled by an overall multiplicative factor (except for the Gaussian component, which, consistently with its background interpretation, is kept fixed in all spectra) does not adequately fit the spectra (null hypothesis probability <0.01)

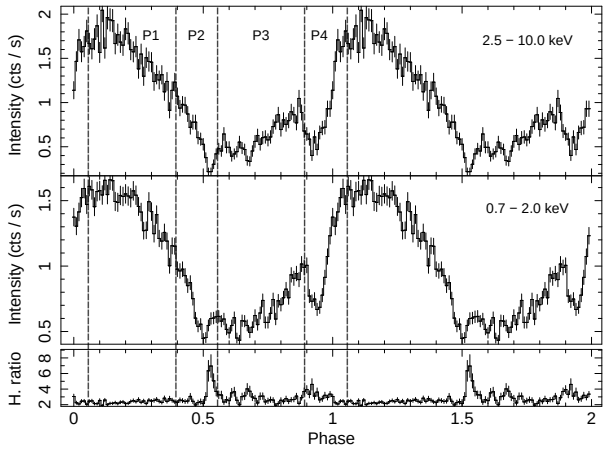

Figure 5. Pulse profile of SWIFT J1822.3-1606 in the 2.5–10 keV interval (upper panel); 0.7–2 keV interval (middle panel) and hardness ratio for those intervals (lower panel). Obs id: 0672281801.

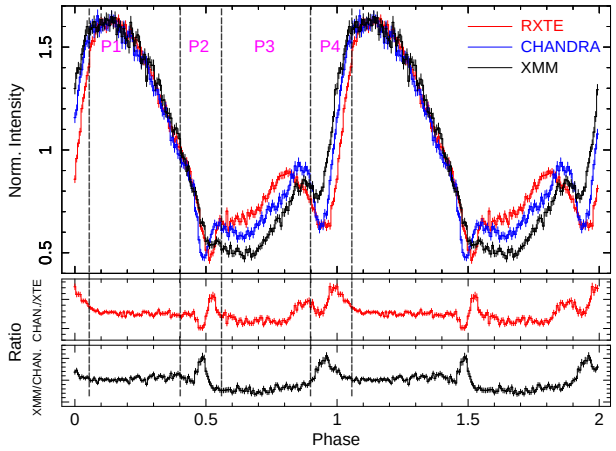

Figure 6. Upper panel: 0.3–10 keV Normalized pulse profiles for the highest statistics light curves which are also a function of increasing time and decreasing flux from the outburst onset: *RXTE*, *Chandra* and *XMM-Newton* in the order of decreasing flux (see also Fig. 3). Lower panels: Ratios of the profiles used to identify the phase interval with larger pulse profile variations.

in the phase intervals 0.03–0.29, 0.49–0.51, and 0.87–0.99. Acceptable fits were obtained by adding a cyclotron absorption line feature (Makishima et al. 1990) to the model in these phase intervals. The resulting line centroids and widths are shown in Fig. 12.

3 RESULTS AND DISCUSSION

We studied the long-term evolution of the magnetar SWIFT J1822.3-1606, by following the source during its approach to quiescence after the outburst that led to its discovery on 2011 July 14. We performed a timing analysis by phase-connecting observations covering about 500 days of the SWIFT J1822.3-1606 outburst decay. The resulting values of the spin period and period derivative are $P = 8.437720019(7)$ s and $\dot{P} = 1.34(1) \times 10^{-13}$ s s^{-1}, which, if interpreted in terms of magneto-dipolar braking, lead to a value of the dipolar magnetic field of $B \sim 3.4(1) \times 10^{13}$ G at the equator of the star. This confirms that SWIFT J1822.3-1606 is the magnetar with the second lowest dipolar magnetic field detected so far. By

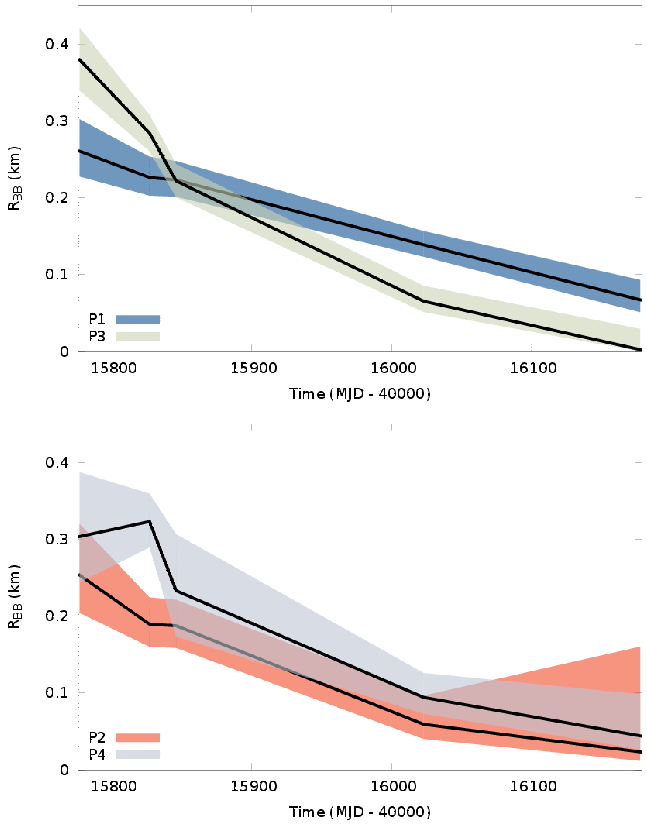

Figure 7. Evolution of the hot blackbodies radii (R_{BB}) used for modeling the pulse phase intervals, see the text for details. The shadows represent the 1-σ confidence interval.

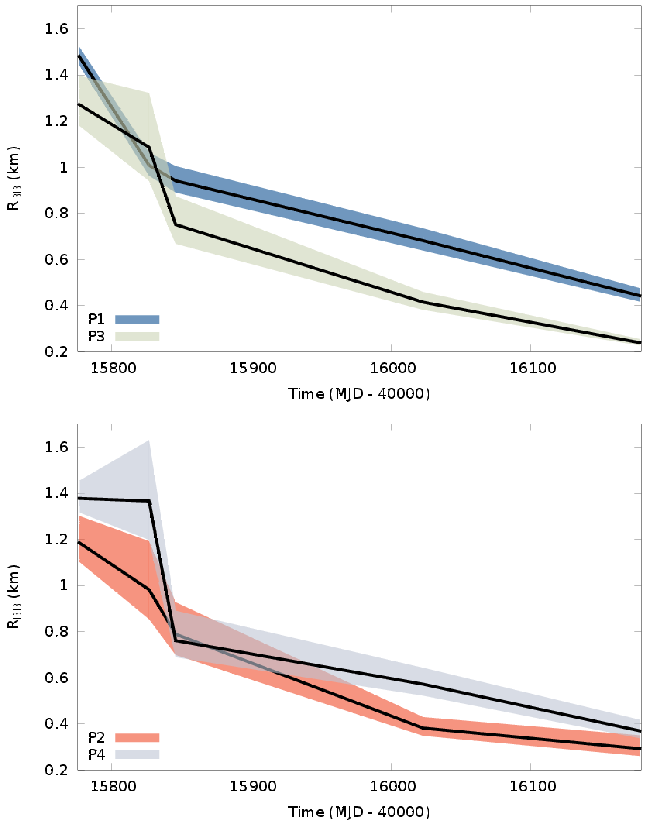

Figure 8. Same as Fig. 7, for the warm blackbodies.

performing a timing analysis, we found a significant second time derivative of the period, $\ddot{P}= -5.1(2) \times 10^{-21}\mathrm{s\,s^{-2}}$, which is consistent with the upper limit reported by R12 and with solution 2 of Scholz et al. (2012); in Scholz et al. (2014) a longer time span is split and fitted with an exponential glitch recovery for the first ~ 60 days and an additional P-$\dot{P}$ solution for the rest of their data set, obtaining a somewhat lower estimate of the dipolar magnetic field of $B \sim 1.4 \times 10^{13}$ G.

A closer look at the PPS results shows however that, apart from the above mentioned common characteristics, the spectral evolution of the source at phase intervals P1 and P3 is markedly different from that observed at P2 and P4. The evolution of the spectra at phase intervals P2 and P4 is very similar (see lower panels of Fig.s 7 – 9) in terms of both measured values of BB radii and temperatures at each epoch, and in terms of shrinking and cooling rates. Instead, spectra observed at phase intervals P1 and P3 have different initial values of the BB radii and temperatures and then display different shrinking and cooling rates over the outburst decay (see upper panels of Fig.s 7 – 9). This may suggest that, during the phase intervals P1 and P3, we are observing two zones with physically distinct properties, likely the two main surface zones that had been heated during the outburst. Instead, during the phase intervals P2 nd P4, we observe a transition, with one of the two heated zones exiting and the second one entering into view. The fact that the temperatures of P2 and P4 are consistently *in between* those of P1 and P3 and that the shape of the observed pulse profile is hardly compatible with a single hot spot, reinforces this two-zones interpretation. We therefore suggest the possibility that the emission is coming from (at least) two zones of the neutron star surface with different physical properties, the evolution of which may be due to different mechanisms. The blackbody radius R_{BB} obtained from our spectral fits may not provide a direct measure of the size L of the emitting region on the star surface. In fact, knowledge of the viewing geometry of the source (i.e. magnetic and spin axis inclinations with respect to the line of sight) and of the location of the emitting regions on the star surface would be required to relate L to R_{BB}. An evaluation of the source geometry will not be attempted here (although this might be possible, see e.g. Albano et al. 2010). We just note that, since these angles are not expected to change during the outburst decay, the time evolution of R_{BB} mirrors that of L, that is to say that the rate of change of the two quantities is the same.

The evolution observed during the decay phase of an outburst is usually interpreted in terms of either the cooling that follows deep crustal heating (Perna & Pons 2011) or untwisting of the star magnetosphere (Beloborodov 2009). The overall behaviour of SWIFT J1822.3-1606 i.e., the shrinking of the heated zones at an almost constant temperature, is expected in the framework of both models. For instance, in the untwisting magnetosphere (UM) model, the twist is initially implanted in a current-carrying bundle of magnetic field lines which then gradually shrinks. Since crustal heating is caused by back-flowing currents in the j-bundle, a decrease in the size of the j-bundle also implies a decrease in the heated surface area (Beloborodov 2009). We also note that the presence of a negative $\ddot{P}$, as follows from our timing analysis, is in agreement with the UM. In fact, immediately prior to the outburst, when the magnetic field of the star is expected to be highly twisted, the star is subject to a large amount of spin-down torque and therefore the spin-down rate is larger with respect to its value in quies-

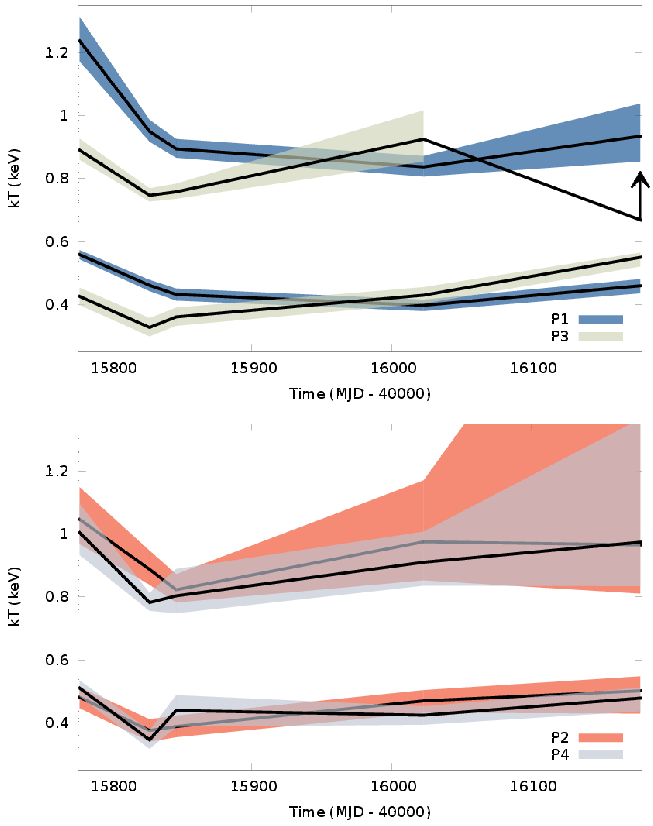

Figure 9. Temperature evolution of the blackbodies used for modeling the pulse phase intervals. Lower values correspond to the warm components, higher values to the hot components. The shadows represent the 1-σ confidence interval.

cence. If, later during the decay, the field untwists, then the spin-down rate should return to the (secular) pre-outburst value. Therefore in this phase a negative second derivative of the spin period should be observed.

To further test the possibility that a surface zone heated by the j-bundle currents is visible at certain phase intervals, we calculated the blackbody emission area and the luminosity corresponding to the hot and warm components observed in the four phase segments. A simple UM model predicts a relation between the luminosity L and the emitting area A of the form $L \propto A^2$ (see Beloborodov 2009). By assuming $L \propto A^n$, for the warm component we found a power law index of $n = 1.6, 1.0, 0.7, 0.9$ in the phase interval P1, P2, P3 and P4 respectively. The correspondent index relative to the hot component are $n = 1.4, 2.3, 1.9, 1.0$. Therefore only some of the measured relations are close to the theoretical expectations. As an example, in Figs. 13 and 14 we show the evolution of the luminosity with respect to the emitting area as observed for the warm component during phase intervals P3 and P1, respectively (the dashed lines represent the relation expected theoretically). As it can be seen, the evolution observed during P1 is compatible with being related to an evolving current-carrying bundle, while the warm component observed during P3, which evolves very differently ($L \propto A^{0.7}$), may be related to a different emission mechanism. The luminosty/area relation detected at P3 is much flatter, and seems to become steeper and steeper as the outburst decay progresses. Our fitting model, which does not allow us to reconstruct the location of these components on the star surface, is however too simplicistic to derive more robust conclusions.

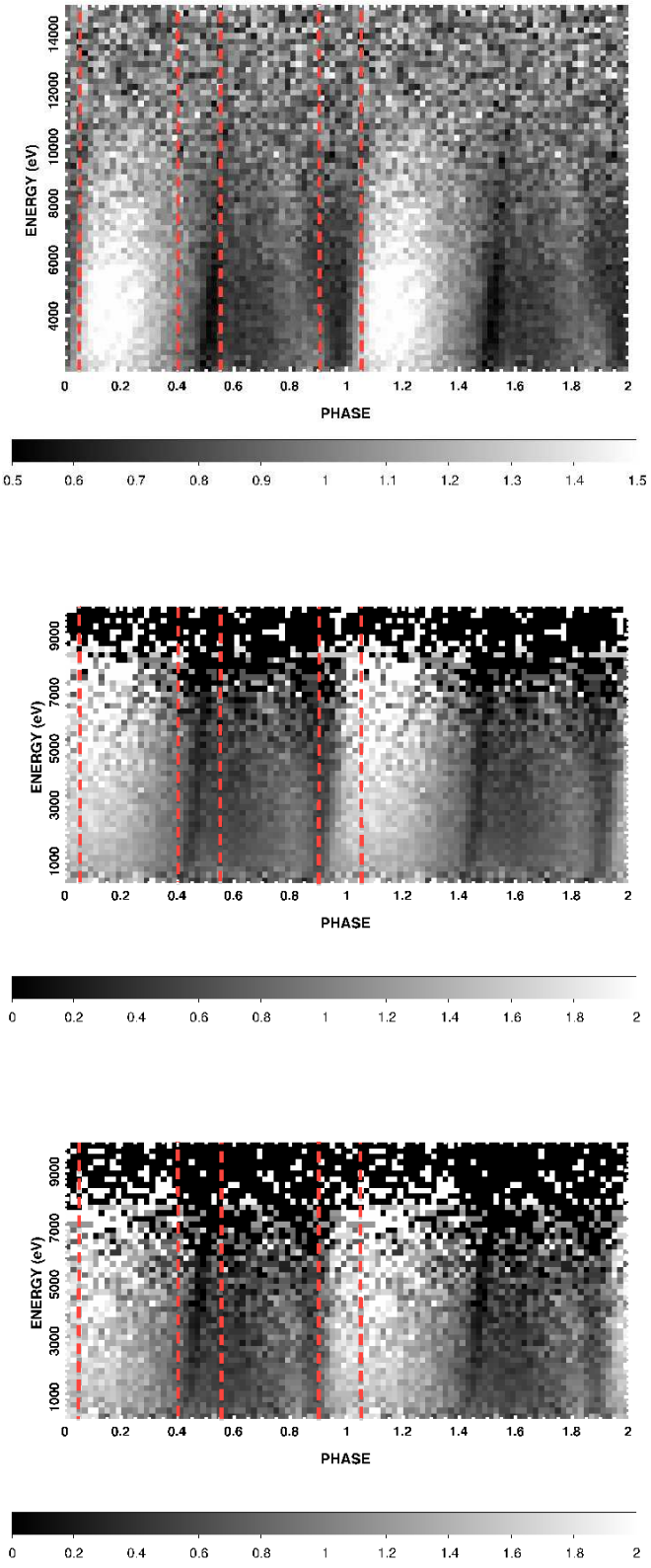

Figure 10. Phase-energy images, divided by the phase-average spectrum, of SWIFT J1822.3-1606 from *RXTE* (PCA observations from 2011 July 16 to 2011 July 20, *top panel*), *Chandra* (ACIS-S observation in CC mode on 2011 July 27, *middle panel*) and *XMM-Newton* (EPIC pn observation on 2011 September 23 *bottom panel*) data. The vertical dashed lines denotate the intervals used in the PPS (see Fig. 6).

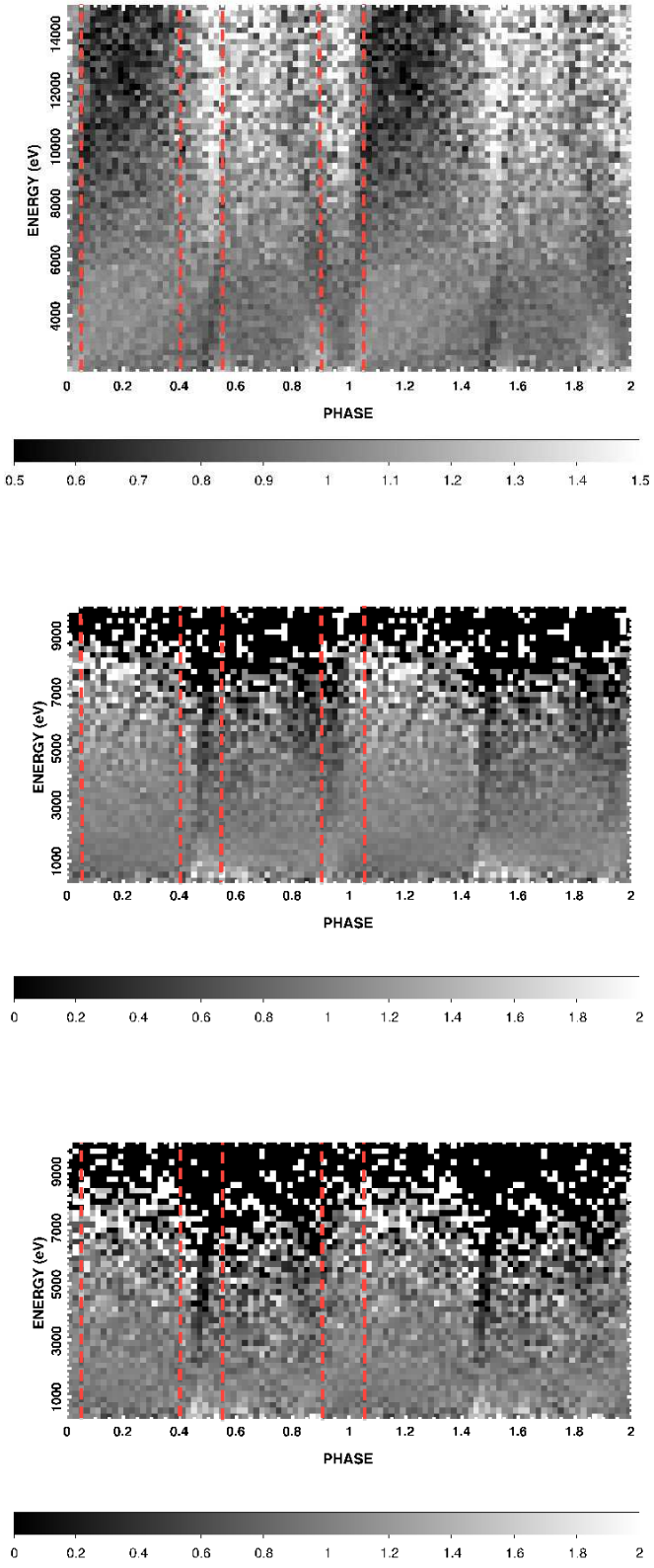

Figure 11. Normalized phase-energy images, divided by the phase-average spectrum and the energy -integrated pulse profile, of SWIFT J1822.3-1606 from *RXTE* (PCA observations from 2011 July 16 to 2011 July 20, *top panel*), *Chandra* (ACIS-S observation in CC mode on 2011 July 27, *middle panel*) and *XMM-Newton* (EPIC pn observation on 2011 September 23 *bottom panel*) data. The vertical dashed lines denotate the intervals used in the PPS (see Fig. 6).

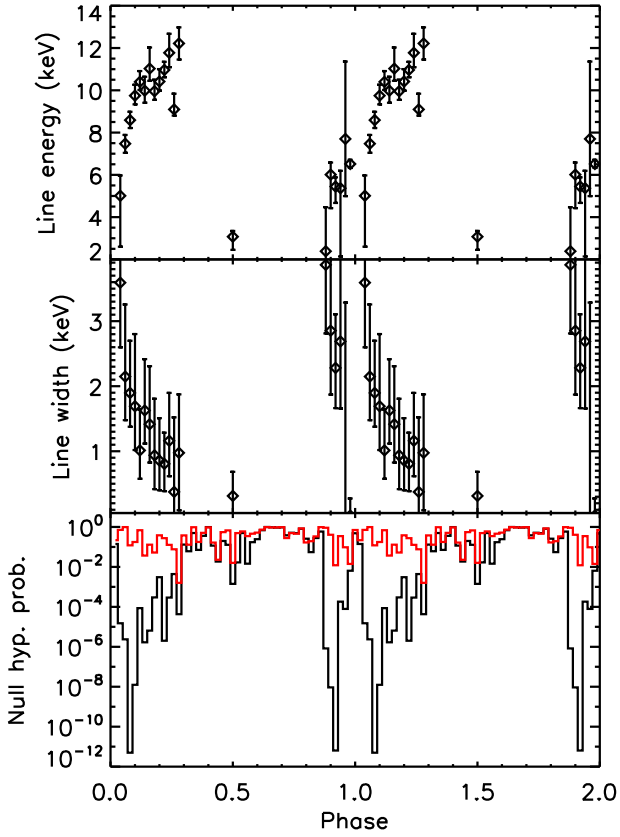

Figure 12. Results of the analysis of 50 phase-resolved spectra of SWIFT J1822.3-1606 during the *RXTE* observations from 2011 July 16 to 2011 July 20. The energy and width of the line is displayed in the upper panels for the phase intervals that were not adequately fit (null hypothesis probability <0.01) by the model without absorption line. The bottom panel shows the null hypothesis probabilities of the fits of each phase-resolved spectrum with the best fit model of the spectrum extracted from the 0.6–0.8 phase interval (see text for details; *black*) and after the addition of an absorption line (*red*).

An particular case is the evolution of the warm temperature relative to the P3 phase interval (Fig. 9, upper panel), which remains (within the 1-σ errors) constant up to the second to last observation. Then in the last observation, the hot BB is not present anymore and the spectrum becomes consistent with a single free BB at ~ 0.5 keV besides the fixed BB at 150 eV (and about 5km of radius). This indicates that in this phase interval at later times only the warm region survives, possibly engulfing the hotter spot. Or, it can be interpreted in terms of the warm BB being slowly heated by the hotter region (hot BB), which dissipates (or shrinks out of the line of sight) as a result.

Fig. 1 shows the flux evolution of the SWIFT J1822.3-1606 during the outburst decay. If we assume the peak luminosity to be of a few 10^{35} erg s^{-1}, as inferred by R12 based on magneto-thermal evolutionary models, it implies a distance to the source of ~ 2 kpc. This is consistent with the distance to the Galactic HII region M17, described in Sec. 2.2; and provides further support for the $N_{\rm H}$ and distance values assumed in this work.

We also reported the detection of a phase and energy-variable spectral line (Figs. 10 and 11). As it can be seen in Fig. 10, a dark V-shaped feature is visible in the RXTE data at phases $\sim$ 0.9-1.1,

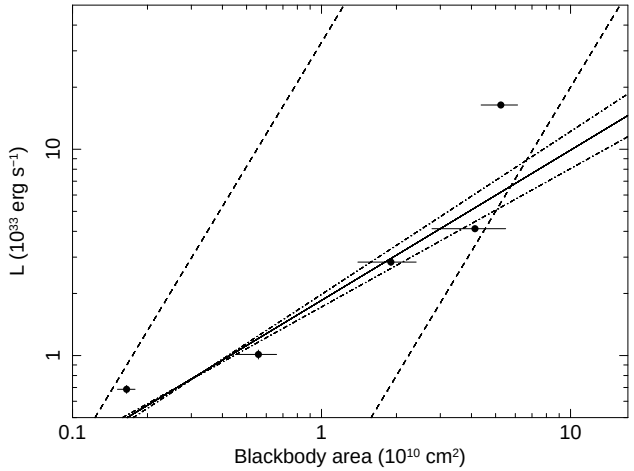

Figure 13. Luminosity versus blackbody emitting area of the P3 warm component (See Fig. 6 for reference). The dashed lines represent $L \propto A^2$, simple untwisting magnetosphere models, see Beloborodov (2009). The solid line is a power-law fit to the data, which yields $L \propto A^{0.7}$. The 3σ uncertainty of the fit parameters is represented by dot-dashed lines.

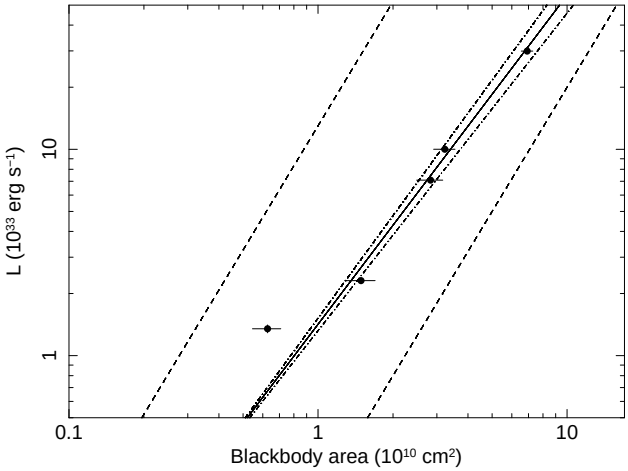

Figure 14. Same as Fig. 13, for P1. The solid line is a power-law fit to the data, which yields $L \propto A^{1.6}$. The 3σ uncertainty of the fit parameters (corresponding to $L \propto A^{1.5}$ and $L \propto A^{1.7}$) is represented by dot-dashed lines.

followed by a dark area around phases 1.2-1.3. The energy of the feature varies between ~ 5 and ~ 12 keV. There is also another feature at lower energy (~ 2 keV) at phase ~ 0.5, which, if significant, may be just a continuation of the main feature (this is supported by the line width evolution but not by the line energy evolution, see the two upper panels of Fig.11). A similar phase and energy dependent feature has been detected so far only in two sources: the low-B magnetar SGR 0418 (see T13) and the X-ray dim isolated neutron star RX J0720.4-3125 (see Borghese et al. 2015). s in these sources the feature may be due to proton-cyclotron resonant scattering of X-ray photons emitted by the star surface onto charges flowing in a small coronal magnetic loop (for alternative interpretations see the discussion in T13 and Borghese et al. 2015). The energy variation of the line would be caused by magnetic field gradients along the coronal loop: as the neutron star rotates, photons directed toward us intercept sections of the loop with different magnetic field intensities. In the rest frame of the emitters, the proton cyclotron energy is $E_{cp} = \hbar eB/m_p c \approx 0.63 B_{14}$ keV, where $B_{14} = B/(10^{14}\mathrm{G})$. Assuming that the line is emitted near the surface of the star, its energy as measured by a distant observer is significantly affected by gravitational redshift. Thus, the magnetic field in the small corona loop can be estimated as $B_{14} = (1+z)E_{obs}/0.63$ keV, where E_{obs} is the observed energy of the line, and $z = 2GM_{NS}/R_{NS}c^2 \approx 0.35$ (using a neutron star mass of $M_{NS} \approx 1.4 M_{\odot}$) and a radius of $R_{NS} \approx 10$ km). In the case of SWIFT J1822.3-1606 (E_{obs} between 3 and 12 keV) the resulting magnetic field in the coronal loop is in the $(6-25) \times 10^{14}$ G range.

We note that the absorption line centroids, as inferred from the RXTE PCA, are predominantly at energies close to the upper bound of both the *XMM-Newton* and *Chandra* spectral ranges, or even higher (Fig. 11, upper panel). Therefore, due to the steep spectrum of SWIFT J1822.3-1606 and the rapid decrease of the response of these instruments at energies above about 6 keV, translating into small count statistics, this feature becomes undetectable. In fact it would be virtually indistinguishable from a a modification of a broad spectral component (such as the hot BB) when observed in the *XMM-Newton* or *Chandra* spectral range.

In the case of SGR 0418+5729 instead, the line phase variability could be better characterized because the line centroid energy extended down to ~ 1 keV, where the *XMM-Newton* effective area has its maximum. Moreover, the effect of cyclotron scattering by currents in a magnetic loop is more pronounced when most of the X-ray radiation is produced by a single hot spot on the magnetar surface, as in SGR 0418+5729 rather than by two different regions, as in SWIFT J1822.3-1606.

The discovery of a second magnetar with a magnetic field in the radio-pulsar range strengthens the idea that magnetars are much more common than expected so far. Dormant magnetars may lurk among unidentified, weak X-ray sources and reveal themselves only when they enter an outburst phase. The detection of phase-variable absorption lines in the spectra of both the low-field magnetars discovered up to now is remarkable, the more given that a similar feature has been observed only in the thermally-emitting neutron star RX J0720.4-3125, which has a comparable dipole field but has not exhibited any magnetar-like behaviour. Whether this is a further proof of a (much suspected) link between magnetars and the seven thermally-emitting isolated neutron stars is still an open issue.

ACKNOWLEDGMENTS

We acknowledge the use of public data from the *Swift*, *XMM-Newton* and *Chandra* data archives. PE acknowledges a Fulbright Research Scholar grant administered by the U.S.–Italy Fulbright Commission and is grateful to the Harvard–Smithsonian Center for Astrophysics for hosting him during his Fulbright exchange.

References

Albano A., Turolla R., Israel G. L., Zane S., Nobili L., Stella L., 2010, The Astrophysical Journal, 722, 788

Anders E., Grevesse N., 1989, Geochimica et Cosmochimica Acta, 53, 197

Asplund M., Grevesse N., Sauval A. J., Scott P., 2009, Annual Review of Astronomy & Astrophysics, 47, 481

Balucinska-Church M., McCammon D., 1992, The Astrophysical Journal, 400, 699

Beloborodov A. M., 2009, The Astrophysical Journal, 703, 1044

Borghese A., Rea N., Coti Zelati F., Tiengo A., Turolla R., 2015, ArXiv e-prints
Cummings J. R., Burrows D., Campana S.and Kennea J. A., Krimm H. A., Palmer D. M., Sakamoto T., Zan S., 2011, The Astronomer's Telegram, #3488
Duncan R. C., Thompson C., 1992, The Astrophysical Journal, 392, L9
Feldman U., 1992, Physica Scripta, 46, 202
Gotthelf E. V., Halpern J. P., Buxton M., Bailyn C., 2004, The Astrophysical Journal, 605, 368
Ibrahim A. I., Markwardt C. B., Swank J. H., Ransom S., Roberts M., Kaspi V., Woods P. M., Safi-Harb S., Balman S., Parke W. C., Kouveliotou C., Hurley K., Cline T., 2004, The Astrophysical Journal, 609, L21
Lodders K., 2003, The Astrophysical Journal, 591, 1220
Mereghetti S., 2008, The Astronomy and Astrophysics Review, 15, 225
Nielbock M., Chini R., Jütte M., Manthey E., 2001, Astronomy and Astrophysics, 377, 273
Pagani C., Beardmore A. P., Kennea J. A., 2011, The Astronomer's Telegram, #3493
Perna R., Pons J. A., 2011, ApJL, 727, L51
Protassov R., van Dyk D. A., Connors A., Kashyap V. L., Siemiginowska A., 2002, ApJ, 571, 545
Rea N., Esposito P., 2011, High-Energy Emission from Pulsars and their Systems, Astrophysics and Space Science Proceedings, p. 247
Rea N., et al., 2012, The Astrophysical Journal, 754, 27
Rea N., et al., 2013, The Astrophysical Journal, 770, 65
Rea N., Viganò D., Israel G. L., Pons J. A., Torres D. F., 2014, ApJL, 781, L17
Rodríguez Castillo G. A., Israel G. L., Esposito P., Pons A., Turolla R., Viganò D., Zane S., 2013, MNRAS, submitted
Scholz P., Kaspi V. M., Cumming A., 2014, ApJ, 786, 62
Scholz P., Ng C.-Y., Livingstone M. a., Kaspi V. M., Cumming A., Archibald R. F., 2012, The Astrophysical Journal, 761, 66
Thompson C., Duncan R. C., 1995, MNRAS, 275, 255
Tiengo A., Esposito P., Mereghetti S., Turolla R., et al. 2013, Nature, 500, 312
Townsley L. K., Feigelson E. D., Montmerle T., Broos P. S., Chu Y.-h., Garmire G. P., 2003, The Astrophysical Journal, 593, 874
Turolla R., Zane S., Pons J. A., Esposito P., Rea N., 2011, ApJ, 740, 105
Wilms J., Allen A., McCray R., 2000, The Astrophysical Journal, 542, 914
Zhou P., Chen Y., Li X.-D., Safi-Harb S., Mendez M., Terada Y., Sun W., Ge M.-Y., 2014, ApJL, 781, L16